First principles study of photoelectric properties of (S, Se) co-doped Si*

CHEN Fusong[1, 2], DU Lingyan[1, 2, *], TAN Xingyi[3, 4], LI Qiang[3]

1. School of Automation and Information Engineering, Sichuan University of Science & Engineering, Zigong 643000, China
2. Artificial Intelligence Key Laboratory of Sichuan Province, Sichuan University of Science & Engineering, Yibin 644000, China
3. College of Intelligent Systems Science and Engineering, Hubei Minzu University, Enshi 445000, China
4. Department of Physics, Chongqing Three Gorges University, Wanzhou 404100, China

Abstract

In order to provide more accurate theoretical guidance for improving photoelectric properties of chalcogens doped silicon, the lattice structure, stability, band structure, density of state and optical properties of (S, Se) co-doped silicon are systematically investigated based on the first principles, and the related properties are compared with those of S-doped and Se-doped silicon. The calculated results show that the photoelectric characteristics of S-doped Si and Se-doped Si are extremely similar to each other, with a new impurity band appearing in their bandgap. This new impurity band primarily results from the contributions of the 3s state electrons of S and the 4s state electrons of Se, promoting the absorption of low-energy photons and increasing the optical absorptivity of doped Si in the near infrared region. Compared with monocrystalline silicon, the S-doped Si and Se-doped Si have the optical absorption spectra, each with a new peak at 0.6 eV, which is caused by the transition of electrons from the impurity band to the conduction band. The (S, Se) co-doped Si exhibits good stability at operating temperature, and two impurity bands appear between the valence

* The paper is an English translated version of the original Chinese paper published in Acta Physica Sinica. Please cite the paper as: CHEN Fusong, DU Lingyan, TAN Xingyi, LI Qiang, First principles study of photoelectric properties of (S, Se) co-doped Si. *Acta Phys. Sin.*, 2025, 74(7): 077101.doi: 10.7498/aps.74.20241434

band and conduction band, which are formed by electrons from the 3s state of S and the 4s state of Se, respectively. The optical absorptivity of (S, Se) co-doped Si is greatly improved in the low energy region compared with that of single doped Si, with a new absorption peak appearing at 0.65 eV, similar to the formation observed in singly doped Si. However, due to the indirect transition process between two impurity energy bands, the absorption peak of (S, Se) co-doped Si is larger in the low energy region. Compared with S-doped silicon and Se-doped silicon with the same concentration, the (S, Se) co-doped Si has optical absorptivity that is significantly improved in the range from 0.81 eV to 1.06 eV. This study provides theoretical guidance for applying the (S, Se) co-doped Si to the field of photoelectron such as infrared photodetectors and solar cells.

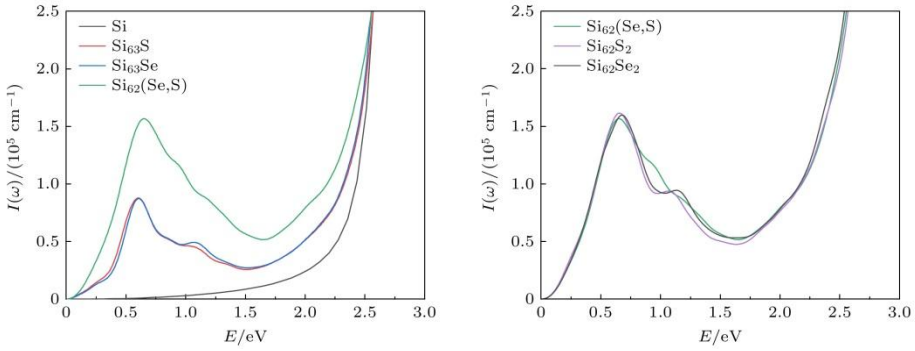

Keywords: doped Si; first principles; photoelectric characteristic
PACS: 71.15.-m; 71.20.-b; 71.55.-i
doi: 10.7498/aps.74.20241434
cstr: 32037.14.aps.74.20241434

1. Introduction

With the advent of the era of big data, high-speed communication and massive data storage have become a difficult problem to be solved[1]. Relying solely on electronics as an information carrier for computing and information transmission, it is difficult to break through the limits of microelectronics technology in terms of delay and power consumption. The emergence of silicon-based optoelectronic technology represents a paradigm shift in information processing, where photons are employed as primary information carriers to facilitate advanced signal transmission and detection functions. Silicon has long been widely used in microelectronics due to its low cost, mature manufacturing processes, and environmentally benign properties. However, its wide bandgap (1.12 eV at room temperature) and high near-infrared/infrared reflectivity result in remarkably low

absorption coefficients within the communication band, significantly limiting its optoelectronic applications. At present, germanium[2], Ⅲ-Ⅴ [3] and other materials sensitive to the infrared region are often used to make near-infrared detectors in the market, but most of these materials have high cost, toxicity, and most importantly, they are not compatible with the existing complementary metal-oxide semiconductor (CMOS) process, which limits their further application in silicon-based optoelectronic devices. If the special impurity energy level can be introduced into monocrystalline silicon by doping to broaden the spectral detection range of silicon-based detectors, it is expected to expand the application range of silicon-based photodetectors. In 1998, Her et al. Reported[4] that the surface of monocrystalline silicon irradiated by femtosecond laser in SF_6 atmosphere could produce micron-scale pyramidal array structure, and the supersaturated doping of sulfur element could be formed in the silicon. This doped silicon was named "black silicon" due to its black surface. In the study on the optical properties of black silicon, Wu et al. [5] reported that this material exhibits an absorptivity exceeding 90% in the near-infrared spectrum. This discovery has attracted great significant academic interest, prompting extensive research efforts over the past two decades to optimize the fabrication of doped silicon and enhance its photoelectric performance. For example, introducing Group VI elements into Si lattices can extend its absorption range to sub-bandgap infrared bands[6–9] , but after thermal annealing, the infrared absorption of doped Si will decrease[6]. Subsequent researchers used a two-step process of etching followed by doping to prepare S-doped micro-nano structure silicon, which successfully ensured that it still had high absorptivity in the near-infrared band even after thermal annealing[8]. Gao Yuchen[10] demonstrated that Si photodetectors doped with inert elements exhibit excellent photoresponsivity at the 1310 nm wavelength. In addition, people have also paid attention to Mo[11], Zn[12], Ⅲ-Ⅴ group[13] and other elements, and the experimental results show that the photoelectric responsivity of infrared detectors prepared by doping silicon with these elements has been significantly improved. Investigating the structure of doped silicon and the underlying mechanisms of its photoelectric properties could provide precise theoretical foundations for optimizing doped-Si fabrication and enhancing its optoelectronic performance. Therefore, extensive theoretical investigations on doped silicon have been conducted by researchers worldwide in recent years[14–20]. As demonstrated by Wang et al.[14] , comparative studies of B/P single-doped and co-doped Si systems revealed that at equivalent doping concentrations, B-doped p-Si exhibits stronger near-infrared absorption than P-doped n-Si; and after impurity compensation in B-P co-doped systems, the near-infrared absorption of n-Si can be enhanced, while p-Si exhibits the opposite trend. Xue et al.[15] calculated the adsorption energy and electronic properties of C-doped Si by first principles, proved that the stability and conductivity of C-Si did not increase monotonously with the increase of C content, and found that the

optimal coverage of C was 0.5. In the experiment of heavily doping Si with different concentrations of Co element, it was found that the maximum doping concentration of Co was $2.601 \times 10^{20} \mathrm{cm}^{-3}$. When the doping concentration was further increased, the doping model showed the whole process of insulator-metal transition. Liang Weihua et al.[16] doped Ni in silicon nanowires and studied the structural stability, electronic properties and optical properties of the material through first principles. The results show that Ni preferentially occupies the substitution sites near the surface of the silicon nanowire, and impurity levels are introduced into the forbidden band of the silicon nanowire, which are mainly contributed by the 3D orbitals of Ni; A strong absorption peak appears in the low energy region of Ni-doped silicon nanowires, accompanied by a broadening of the absorption band. VI group elements are the symbolic doping elements of black silicon structure, and a large number of experimental studies have been carried out around them, but the study of the photoelectric properties of VI group element co-doped Si is relatively shallow both in theory and experiment. Therefore, this work applies density functional theory with PAW pseudopotentials to examine S/Se doping effects in silicon. The research focuses on the structural stability, electronic characteristics, and optical responses of both single-doped and co-doped Si configurations. Through comparative analysis of these chalcogen-doped systems, we aim to explore the internal mechanism underlying doping-induced optoelectronic property modulation in silicon, so as to provide a theoretical reference for experimental work.

2. Model Construction and Calculation Method

2.1 Model construction

Initial structures were constructed using hexagonal A4-type silicon with space group $Fd3m$, lattice constants $a = b = c = 0.543$ nm, and interfacial angles $\alpha = \beta = \gamma = 90$ °. A 2 × 2 × 2 supercell containing 64 atoms was employed to simulate S and Se doping configurations, including both single-element doping and co-doping systems. For the single-doping models, one Si atom was replaced by either S or Se dopant, as shown in Fig. 1, achieving a dopant concentration of 1.56%. For the co-doping model, S and Se dopants were strategically positioned to minimize their mutual interactions as shown in Fig. 2, resulting doping concentration of 3.12%.

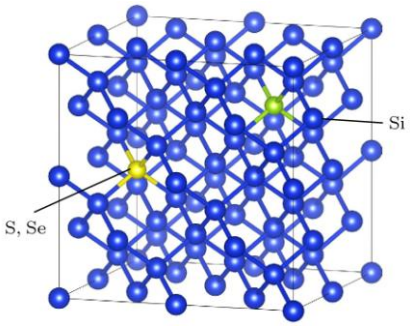

Figure 1. Schematic diagram of S and Se single doping model.

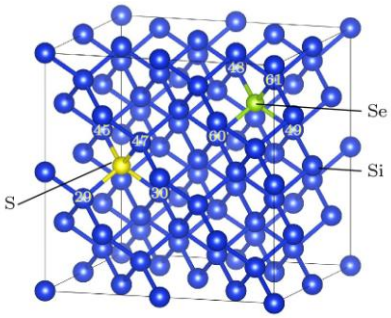

Figure 2. Schematic diagram of the co-doping model of S and Se (Numbers represent Si atomic number).

2.2 Calculation method

In this paper, first-principles calculations based on density functional theory (DFT) were carried out for S, Se co-doped silicon system by using VASP software, and compared with S, Se single-doped model. The Perdew-Burk-Emzerhof (PBE) [21] in the generalized gradient approximation (GGA) was used to describe the exchange-correlation function. Electron-ion interactions were modeled with the projector augmented plane wave (PAW)[22] pseudopotential method, while temperature control in the canonical ensemble (NVT) molecular dynamics simulations was achieved through the Shuichi[23] thermostat.

In the calculation, the structure of the established model was optimized to obtain the optimal geometric structure, and then the single-point energy and properties were calculated. Calculations employed a 330 eV plane-wave cutoff, 1 fs timestep, 1.0×10^{-8} eV energy convergence threshold, and atomic force convergence criterion of 0.02 eV/Å. the energy calculation was done in reciprocal space, the k point network was taken to be 3 × 3 × 3, and the spin polarization was not considered in the calculation.

3. Computational structural analysis and discussion

3.1 Lattice constant and formation energy

In order to compare the changes of lattice constants and bond lengths of Si before and after doping, the structures of primitive Si unit cell, Si (2 × 2 × 2) supercell, $Si_{63}S$, $Si_{63}Se$ and Si_{62} (Se, S) were optimized respectively. The optimized structural parameters are shown in Tab. 1. Notably, the optimized lattice constant of the primitive Si unit cell exhibits a marginal 0.7% expansion compared to its initial value, which is characteristic of GGA employed for exchange-correlation energy calculations. In general, the lattice constant and molecular bond length calculated by GGA are slightly increased[24]. The data in the table further demonstrate that the S-doped supercell exhibits the smallest lattice constant, relative to the pure silicon supercell, while the lattice constant variant of Se-doped supercell exhibits the largest. This phenomenon directly correlates with the covalent radii of dopant atoms: S (1.00 Å) < Si (1.11 Å) < Se (1.15 Å). The comparative analysis reveals that all Si-X bonds (X = S, Se) demonstrate significant elongation compared to both the intrinsic Si-Si bonds within the same unit cell and those in monocrystalline silicon. Specifically, the bond length follows the order: Si-Se > Si-S > Si-Si, which directly correlates with the ionic radii of the dopant species (S^{2-}: 1.84 Å; Se^{2-}: 1.98 Å) being substantially larger than silicon's covalent radius.

Table 1. Lattice constants and bond lengths of single crystal silicon, Si supercell, S, Se single doping and co-doping silicon after structure optimization.

Compound	Lattice constant/Å	Bond length/Å		E^f /eV
		Si—*X*	Si—Si	
Si single unit cell	5.467	—	2.367	—
Si（2×2×2）	10.934	—	2.367	—
$Si_{63}S$	10.928	2.463	2.365	1.24
$Si_{63}Se$	10.946	2.558	2.368	1.27
Si_{62}(Se, S)	10.944	2.457(Si—S) 2.552(Si-Se)	2.364 2.367	2.54

To systematically investigate the thermodynamic stability of S and Se elements in the silicon matrices, the impurity formation energy for S and Se doped Si supercells was further calculated, and the calculation formula of the formation energy $E^{\mathrm{f}}[\mathrm{Si}_n X]$ was[25].

$$E^{\mathrm{f}}[\mathrm{Si}_n X] = E[\mathrm{Si}_n X] - E[X] - \frac{n}{n+1} E[\mathrm{Si}_{n+1}], \quad (1)$$

Where $E[\mathrm{Si}_n X]$ denotes the total energy of the doped crystal, $E[X]$ corresponds to the ground-state energy of isolated X element, and $E[\mathrm{Si}_{n+1}]$ represents the total energy of primitive silicon system containing n+1 atoms. As quantitatively demonstrated in Table 1, The calculated formation energies demonstrate that both S/Se singly doped Si and (S, Se) co-doped silicon systems follow a consistent trend: larger dopant radii and higher concentrations lead to greater incorporation difficulties and consequently higher formation energies.

3.2 Kinetic property

The stability of a material plays a decisive role in its practical application. In order to explore the stability of $(\mathrm{S}, \mathrm{Se})$ co-doped silicon structure under operational conditions, the dynamic simulations of the co-doped material structure were performed at 298 K. Fig. 3 illustrates the temporal evolution of bond lengths between the dopant atoms (S/Se) and their four neighboring Si atoms, demonstrating the co-doped system maintains dynamic stability within a localized region. Furthermore, the root mean square deviation (RMSD) of S/Se atoms from their initial position in the co-doping configuration is calculated to measure the degree of deviation of the atoms from the average position:

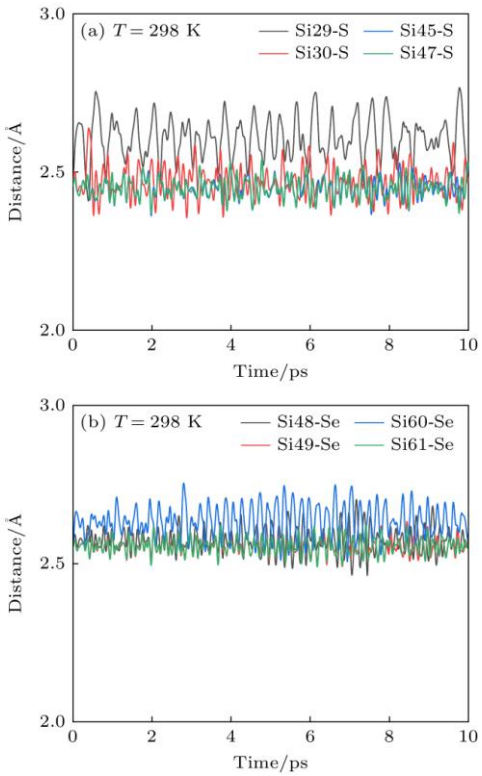

Figure 3. Plot of the bond length of S (a) and Se (b) atoms with the surrounding Si atoms as a function of time.

$$\mathrm{RMSD}_{\alpha}(t) = \sqrt{\frac{1}{N_{\alpha}} \sum_{\alpha=1}^{N_{\alpha}} (r_{\alpha}(t) - \langle r_{\alpha} \rangle)^2}, \tag{2}$$

Where N_{α} is the number of atoms; $r_{\alpha}(t)$ is the position of atom α at time t; $\langle r_{\alpha} \rangle$ is the average position of atom α in the whole time period, which is formulated as

$$\langle r_{\alpha} \rangle = \frac{1}{N_{\mathrm{t}}} \sum_{1}^{N_{\mathrm{t}}} r_{\alpha}(t), \tag{3}$$

In the formula, N_{t} is the whole time period. Fig. 4 presents the temporal evolution of RMSD for S and Se atoms, demonstrating the deviation of S and Se atoms from the average position is small and stable within a certain range, which further proves the stability of the S and Se co-doped model theoretically.

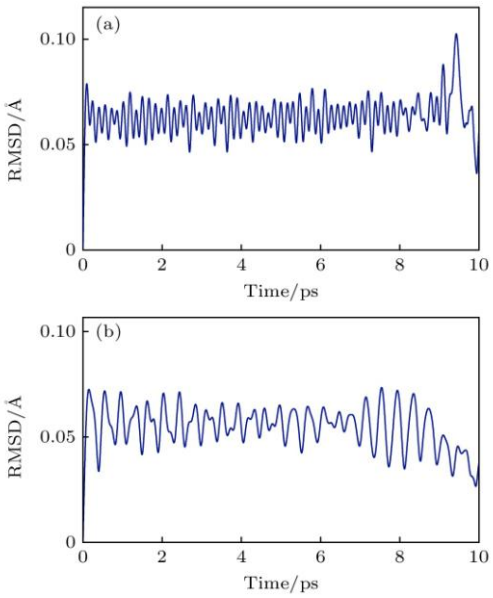

Figure 4. Plot of the RMSD of the position offset of S (a) and Se (b) atoms as a function of time.

3.3 Analysis of electronic structure properties

The photoelectric performance of semiconductor materials is fundamentally dominated by their electronic band structure and density of states (DOS). As revealed in Fig. 5 and Fig. 6, comparative analysis of the band structures and total density of states near the Fermi level clearly demonstrates the electronic structure modulation induced by (S, Se) co-doping in silicon, with systematic comparison to single-dopant configurations. It can be seen from the Fig. 5(a) that Si is an indirect band gap semiconductor with a band gap width of 0.6098 eV, which is very close to the calculation result (0. 6 eV) obtained by reference [26], but far from the experimental value (1. 12 eV). This is a common problem in first-principles calculations, which is mainly due to the overestimation of the repulsion between valence electrons in the generalized gradient approximation, which enlarges the width of the valence band and squeezes the width of the forbidden band gap[27]. However, this does not affect the analysis and comparison of the experimental results, and can still provide guidance for the experiment. Fig. 6 reveals a distinct DOS peak at 1. 17 eV in S, Se singly doped Si, which remarkably disappears in the co-doped system. This suppression effect originates from the elevated impurity concentration in co-doped systems, where intensified electron-impurity ion scattering causes delocalization of electronic states across the energy space, consequently eliminating the DOS peak. To validate this hypothesis, the single doping structure with the same concentration as the co-doping is constructed with subsequent charge density of States calculations. As shown in the Fig. 7, at 1.17 eV, the single doping Si with 3.12% concentration of S or Se also

lacks the peak of density of States. In addition, the intermediate band of 3.12% doped Si is wider than that of 1.56% doped Si. This phenomenon arises from the elevated doping concentration, which enhances the hybridization probability both among impurity bands themselves and between impurity bands and the conduction band minimum (CBM), thereby altering the shape and width of the intermediate band. Fig. 8 presents the partial density of States (PDOS) of Si both before and after doping. Comparing Fig. 5(a) and Fig. 8(a), it can be seen that from –2 eV to 0 eV is primarily formed by the Si 3p states, while the conduction band from 0.6 eV to 2 eV contains contributions from both Si 3s and Si 3p states. This is consistent with the total density of States of Si shown in Fig. 6. From Fig. 5(b) and (c), it is evident that after single doping S or Se, the Fermi level of Si material relocates upwards into the expanded conduction band containing impurity level. This relocation is caused by the increase of electrons after impurity incorporation. Furthermore, an impurity level appears within band gap, formed by the interaction of 3s state and 3p state of S, 4s state and 4p state of Se after S and Se doping. And because both S and Se belong to Group VI elements, the doped Si materials show similar electronic structure characteristics, which aligns well with the total density of States of S or Se single doped Si shown in Fig. 6. As evidenced in Fig. 8(b)-(e), the valence band of S or Se single doped Si receives contributions not only from the original Si 3p states but also from S 3p states (for S doping) and Se 4p states (for Se doping). In the conduction band region, electronic contributions primarily originate from S 3p states and Se 4p/3d states, with additional participation from Si 3s and 3p states. There are two impurity bands in Fig. 5(d), which correspond to the incorporation of S and Se. Compared to monodoping cases, these impurity levels exhibit significant energy fluctuations, aligning with the total density of states analysis presented earlier. Based on Fig. 8(f)-(h), the PDOS of (S, Se) co-doped Si demonstrates compositional similarities to S/Se single doped models: the valence band involves Si 3p, S 3p, and Se 4p states; the conduction band primarily comprises S 3p and Se 4p states, with additional components from Si 3s/3p, S 3s, and Se 4s/3d states. The intermediate impurity band is predominantly formed by S 3s and Se 4s states, with secondary participation from S 3p and Se 4p orbitals.

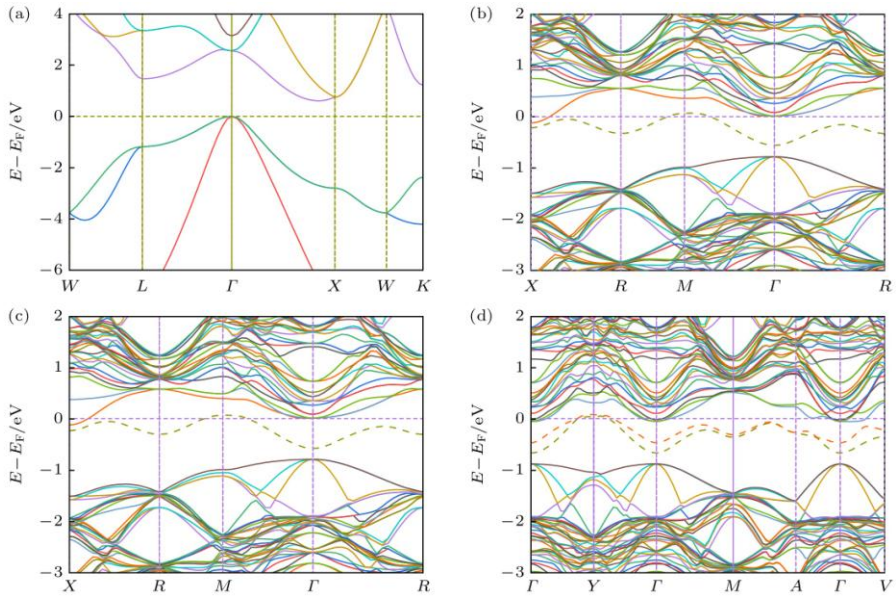

Figure 5. Band structure of pure Si and doped Si: (a) Si; (b) $Si_{63}S$; (c) $Si_{63}Se$; (d) Si_{62}(Se, S).

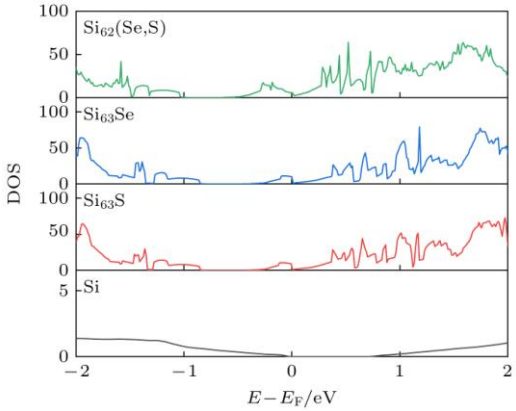

Figure 6. Total density of states of pure Si and doped Si.

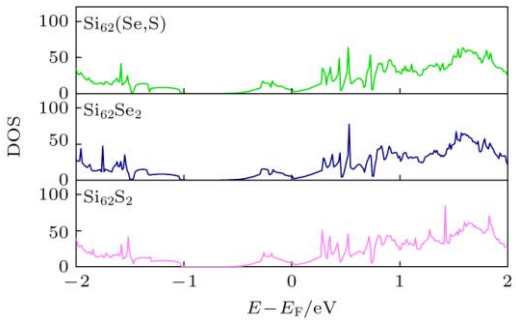

Figure 7. Total density of states of single and co-doped Si at the same concentration.

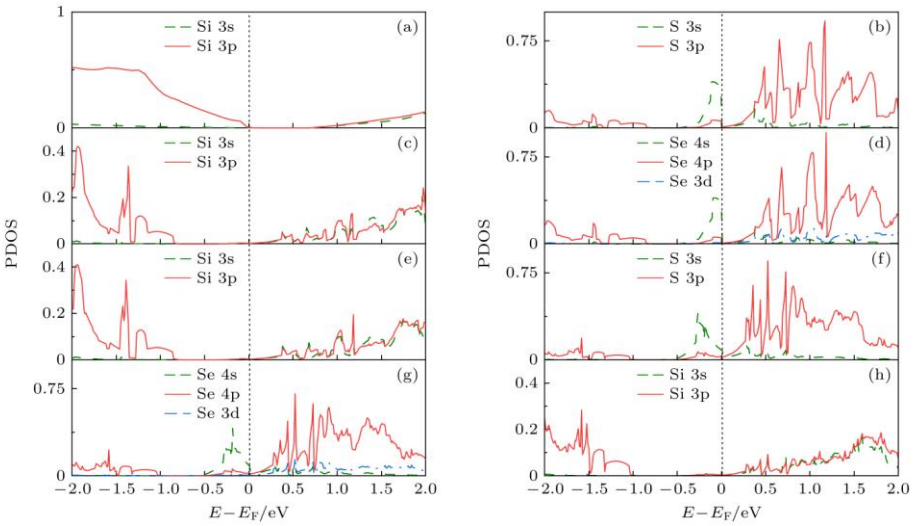

Figure 8. Partial density of state of pure Si and doped Si: (a) Si in pure Si; (b) S in $Si_{63}S$; (c) Si in $Si_{63}S$; (d) Se in $Si_{63}Se$; (e) Si in $Si_{63}Se$; (f) S in $Si_{62}(Se, S)$; (g) Se in $Si_{62}(Se, S)$; (h) Si in $Si_{62}(Se, S)$.

3.4 Optical property analysis

The VASP software package is used to study the optical properties of materials based on the dielectric function $\varepsilon(\omega) = \varepsilon_1(\omega) + \mathrm{i}\varepsilon_2(\omega)$, where the imaginary part of the dielectric function $\varepsilon_2(\omega)$ can be obtained from the (4) expression[28,29], and the real part of the dielectric function $\varepsilon_1(\omega)$ can be obtained from the Kramers-Kronig dispersion relation. Then the optical absorption coefficient $I(\omega)$, the reflectivity $R(\omega)$, the extinction coefficient $K(\omega)$ and the energy loss function $L(\omega)$can be derived from (5)- (8):

$$\varepsilon_2(\omega) = \frac{4\pi^2}{m^2\omega^2}\sum_{v,c}\int_{\mathrm{BZ}} \mathrm{d}^3 k \frac{2}{(2\pi)}|eM_{\mathrm{CV}}(K)|^2 \times \delta[E_{\mathrm{C}}(K) - E_{\mathrm{V}}(K) - h\omega], \tag{4}$$

$$I(\omega) = \sqrt{2}\omega[\sqrt{\varepsilon_1^2(\omega) + \varepsilon_2^2(\omega)} - \varepsilon_1(\omega)]^{1/2}, \tag{5}$$

$$R(\omega) = |\frac{\sqrt{\varepsilon_1(\omega)+\mathrm{j}\varepsilon_2(\omega)}-1}{\sqrt{\varepsilon_1(\omega)+\mathrm{j}\varepsilon_2(\omega)}+1}|^2, \tag{6}$$

$$K(\omega) = [\frac{\sqrt{\varepsilon_1^2(\omega)+\varepsilon_2^2(\omega)}-\varepsilon_1(\omega)}{2}]^{1/2}, \tag{7}$$

$$L(\omega) = \varepsilon_2(\omega)/[\varepsilon_1^2(\omega) + \varepsilon_2^2(\omega)], \tag{8}$$

Where V and C denote the valence band and conduction band, respectively, Bz corresponds to the first Brillouin zone $|eM_{\mathrm{CV}}(K)|^2$ is the momentum transition matrix element, $E_{\mathrm{C}}(K)$ and $E_{\mathrm{V}}(K)$ represent the intrinsic energy levels on the conduction band

and valence band, respectively. The expression involves Dirac constant h, angular frequency ω, and reciprocal lattice vector K.

Fig. 9 displays the imaginary part of the dielectric function of monocrystalline Si and doped Si. Fig. 9(a) reveals that crystalline Si exhibits nearly negligible $\varepsilon_2(\omega)$ values in the 0-1.57 eV range, with three characteristic peaks at 3.71 eV, 4.60 eV, and 6.75 eV, respectively. The peaks at 3.71 eV and 4.6 eV are mainly caused by the electronic transitions between the valence band maximum (VBM) and the conduction band minimum (CBM), while the 6.75 eV peak originates from interband transitions between the valence band at – 6.5 eV and the conduction band minimum. In Fig. 9(b)- (c), S/Se single doped Si exhibits enhanced $\varepsilon_2(\omega)$ in the 0-1.57 eV range and a new peak at 0.55 eV, which is due to the fact that most of the electrons of 3s state of S and 4s state of Se are near the Fermi level and the valence band electrons obviously move to low energy. It is not difficult to conclude that the peak at 0.55 eV is caused by the transition between S 3s→3p and Se 4s→4p states. The three remaining peaks persist at 3.67 eV, 4.45 eV, and 6.29 eV with minor energy shifts relative to those in crystalline Si. As shown in the Fig.9 , that the $\varepsilon_2(\omega)$ peaks of single doped Si at 3.67 eV and 4.45 eV are obviously weakened. This attenuation occurs because these transitions originate from VBM→CBM excitations, and doping-induced Fermi level shifting toward the conduction band depletes electrons near the VBM, thereby reducing transition probability. Obviously, the 6.29 eV peak remains essentially unaffected, and all three peaks exhibit a systematic redshift. In Fig. 9(d), the $\varepsilon_2(\omega)$ of (S, Se) co-doped Si exhibits stronger intensity within 0-1.57 eV, featuring a distinct peak at 0.53 eV. This behavior shares the same origin as single doped cases, while the enhanced intensity stems from interactions between S and Se dopants, which consistent with the total density of states in Fig. 6. The three remaining peaks emerge at 3.66 eV, 4.37 eV and 6.29 eV, respectively, which are similar to those of single doping cases. However, the peaks are quite different from those of single doping. The peaks of the three peaks are obviously weakened, and the peak at 4.37 eV almost disappears, and all of them have a tendency to move to the low energy direction, which is consistent with the situation of single doping, and is related to the Fermi level close to the conduction band.

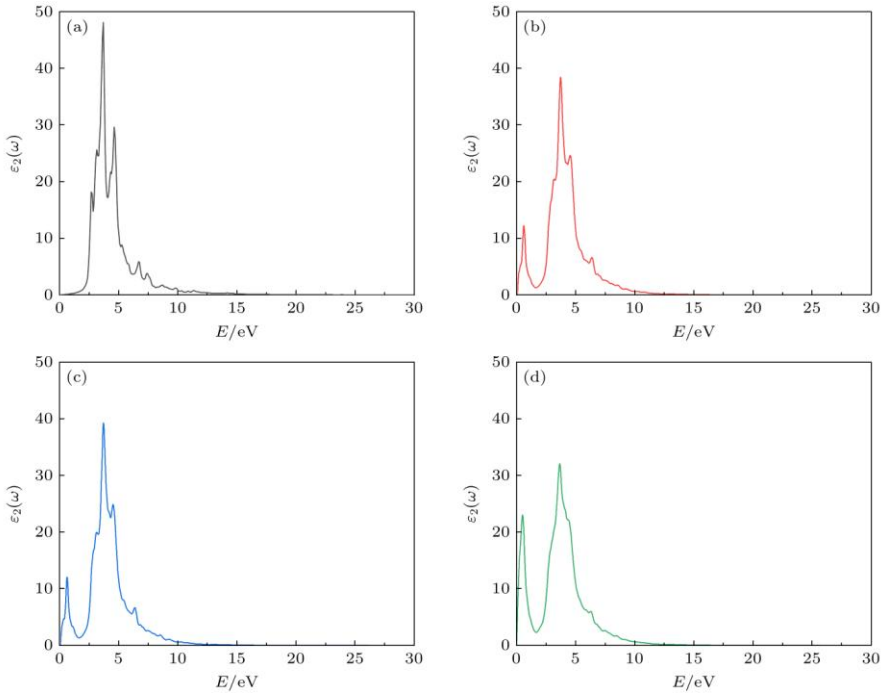

Figure 9. Imaginary part of the pure Si and doped Si dielectric function: (a) Si; (b) $Si_{63}S$; (c) $Si_{63}Se$; (d) Si_{62}(Se, S).

The Fig. 10 presents the absorption spectrum, reflection spectrum, extinction coefficient spectrum and energy loss spectrum of Si before and after doping. As shown in the inset of the Fig. 10(a), intrinsic crystalline silicon exhibits near-zero absorption coefficients in the 0–0.6 eV range. This results from the inherent bandgap underestimation by the PBE functional, which shifts the material's absorption edge toward lower energies. Significantly, both S- and Se- single doped silicon demonstrate nearly identical absorption profiles, remarkably enhanced absorption across 0–1.16 eV, and a strong peak at 0.6 eV. These modifications originate from the Fermi level and impurity levels shift toward the conduction band minimum due to the incorporation of S and Se, collectively facilitating low-energy electronic transitions. The photoexcitation scheme of S/Se singly doped Si in the near-infrared region is shown in the Fig.11. The peak of (S, Se) co-doped Si in the low energy aligns with that of single doped models, but exhibits enhanced intensity at 0. 65 eV. To explore the influence of doping concentration, the absorption spectrum of single doped Si with doping concentration of 3. 12% were further calculated, as shown in the Fig.12. Remarkably, (S, Se) co-doped Si demonstrates substantially enhanced absorption within 0.81–1.06 eV, precisely corresponding to the standard telecommunication window (1170–1530 nm). Analysis of Fig.8(f) and (g) reveals that the impurity band peak induced by S and Se in the co-doping silicon are positioned at – 0.27 eV and – 0.19 eV below the Fermi level, respectively. However, for the single doping cases as shown in the Fig.8(b) and (d), the impurity band peaks induced by S and Se are positioned at – 0.1 eV

and – 0.09 eV below the Fermi level, respectively. Analysis reveals that (S, Se) co-doping not only enlarges the band gap of Si, but also increases the energy separation between impurity levels and the conduction band minimum through (S, Se) interactions, inducing a blue shift in the low-energy absorption peak. In addition, (S, Se) co-doping introduces dual impurity bands that significantly enhance electron transition probabilities, thereby boosting the near-infrared absorption coefficient. Furthermore, during electron transitions from the S-derived impurity band to the conduction band, the stepwise pathway via the Se impurity band (S-band → Se-band → CBM) facilitates low-energy photon absorption through Se-mediated indirect transitions. Consequently, we attribute the enhanced absorption coefficient of (S, Se) co-doped Si in the 0.81–1.06 eV range to this indirect transition mechanism, the corresponding photoexcitation scheme in the near-infrared region is shown in Fig.13. In Fig.10(b), the reflectivity of doped Si exhibits systematically higher reflectivity across the 0–1.16 eV range compared to pure Si, while displaying an opposite spectral evolution in the low-energy region, and the change is more obvious after co-doping. Combined with Fig.10(a), the absorption coefficient and reflectivity of pure Si are low in the low energy region, which proves its high transmittance in the near infrared band. The extinction coefficient in Fig.10(c) is very similar to the optical absorption coefficient, because the extinction coefficient and the optical absorption coefficient can be converted to each other by the formula. Energy loss is a physical quantity that describes the energy loss of electrons when they pass through a uniform dielectric, while the energy loss peak describes the resonance frequency of a plasma. It can be seen from the Fig.10(d) that the energy loss peaks of doped Si are all at 16. 1 eV, while pure Si displays two energy loss peaks at 16. 5 eV and 17. 2 eV, respectively. And the rapid decline of the energy loss peak corresponds to reflectance variations observed in the Fig.10(b). At the same time, the energy loss peak of (S, Se) co-doped Si is lower than that of single doping, S doping is the highest, and Se doping is in the middle.

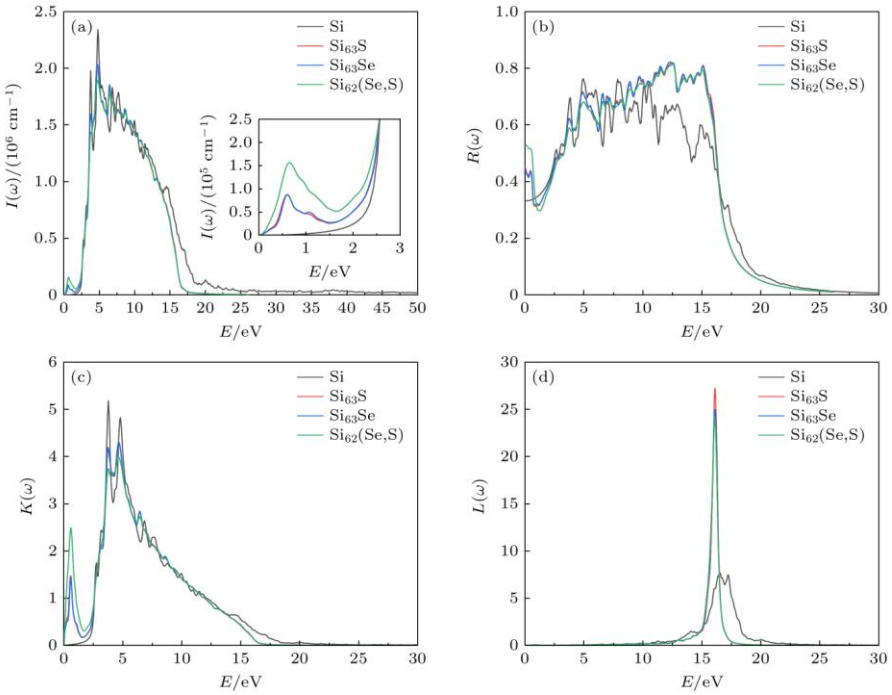

Figure 10. Optical absorption spectrum (a), reflection spectrum (b), extinction coefficient spectrum (c) and energy loss spectrum (d) of pure Si and doped Si, the inset in panel (a) shows the amplification of the optical absorption spectrum of pure Si and doped Si at 0–3 eV.

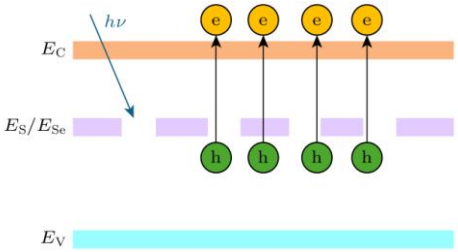

Figure 11. Schematic of the photoexcitation of S and Se single-doped Si in the NIR region.

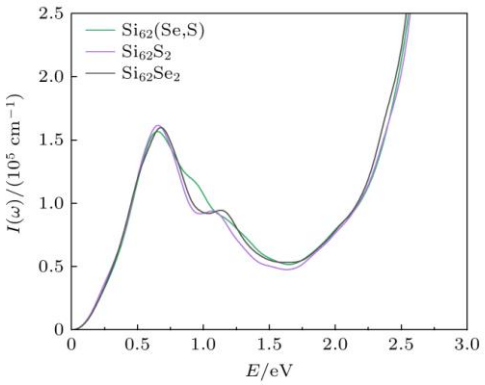

Figure 12. Optical absorption spectra of single and co-doped Si at the same concentration in the near infrared region.

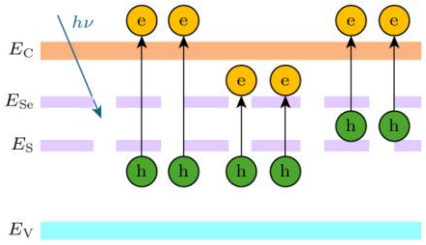

Figure 13. Schematic of the photoexcitation of S and Se co-doped Si in the NIR region.

4. Conclusion

In this paper, the crystal structure, stability, electronic and optical properties of S/Se single doped Si and (S, Se) co-doped Si are investigated based on DFT. The results show that doping shifts the Fermi level upward into the impurity-level-expanded conduction bands, introduces one impurity level near the conduction band minimum for singly-doped Si versus two such levels for co-doped Si, which is mainly formed by the 3s state of S and the 4s state of Se, and also includes the 3p state of S and the 4p state of Se. In terms of optical properties, key distinctions emerge in the low-energy region. The calculation results of the imaginary part of the dielectric function show reduced peaks at 3. 71 eV and 4. 6 eV due to the Fermi level of doped Si close to the conduction band, yet simultaneously exhibits new prominent absorption peaks at 0.55 eV for singly-doped Si and at 0.53 eV for co-doped Si. and the peak of co-doped Si is higher owing to the synergistic effect of S and Se. The optical absorption coefficient and reflectivity of pure Si are low in the low energy region, which proves its high transmittance in the infrared region. The optical absorption coefficient of doped Si is higher than that of pure Si in the low energy region, which just makes up for the low absorption rate of pure Si in the infrared region, and (S, Se) co-doped Si also shows superior absorption within 0.81–1.06 eV compared to concentration-equivalent singly-doped systems, thereby indicating promising potential for infrared detection and solar cell applications.

References

[1] Zhou Z P 2014 *Proceedings of Wuhan Opto-Electronic Forum* （Wuhan: Huazhong University of Science & Technology Press） p249

[2] Michael O, Mathias K, Steffen E, Maurice W, Zili Y, Daniel S, Köllner A C, Joachim N B, Jörg S 2021 *IEEE Sens. J.* **20** 18696

[3] Yang J J, Jurczak P, Cui F, Li K S, Tang M C, Billiald L, Beanland R 2019 *J. Cryst. Growth* **514** 109

[4] Her T H, Finlay R J, Mazur E, Wu C, Deliwala S 1998 *Appl. Phys. Lett.* **73** 1673

[5] Wu C, Crouch C H, Zhao L, Carey J E, Younkin R, Levinson J A, Mazur E, Farrell R M, Gothoskar P, Karger A 2001 *Appl. Phys. Lett.* **78** 1850

[6] Tansel T, Aydin O 2024 *J. Phys. D* **57** 295103

[7] Zhao X N, Lin K, Zhao B, Du W H, Nivas J J, Amoruso S, Wang X 2023 *Appl. Surf. Sci.* **619** 156624

[8] Zhong H 2019 *M. S. Thesis* （Chengdu: University of Electronic Science and Technology of China

[9] Du L Y, Yin J, Zeng W, Pang S Z, Yi H 2023 *Mater. Lett.* **331** 133463

[10] Gao Y C 2022 *M. S. Thesis* （Jilin: Jilin University)

[11] Yang Y, Yi Z R, Chao L, Zhao J H 2023 *Opt. Quantum Electron.* **55** 259

[12] Ren Z Y 2024 *M. S. Thesis* （Jilin: Jilin University

[13] Zhu J, Gandi N A, Schwingenschlögl U 2018 *Adv. Theor. Simul.* **1** 1800017

[14] Wang X Y, Wang T, Ren Q, Xu J T, Cui Y A 2023 *Micro Nanostruct.* **184** 207695

[15] Xue X W 2018 *M. S. Thesis* （Dalian: Dalian University of Technology

[16] Liang W H, Ding X C, Chu L Z, Deng Z C, Guo J X, Wu Z H, Wang Y L 2010 *Acta Phys. Sin.* **59** 8071

[17] Tang X, Li W, Xu W, Ren Q Y, Chen Q Y 2024 *Mater. Sci. Semicond. Process.* **184** 108797

[18] Wu M, Cai G K, Li Z, Ye L, Wang C 2024 *Vacuum* **225** 113222

[19] Li J Y, Zhao C L, Li W, Ren Q Y, Xu J, Xu W 2023 *Phys. Scr.* **98** 115408

[20] Sharif M N, Yang J S, Zhang X K, Tang Y H, Yang G, Wang K F 2024 *Vacuum* **219** 112714

[21] Perdew J P, Burke K, Ernzerhof M 1996 *Phys. Rev. Lett.* **77** 3865

[22] Kresse G, Furthmüller J 1996 *Comput. Mater. Sci.* **6** 15

[23] Shuichi N 1984 *J. Chem. Phys.* **81** 511

[24] Guan L, Li Q, Zhao Q X, Guo J X, Zhou Y, Jin L T, Geng B, Liu B T 2009 *Acta Phys. Sin.* **58** 5624

[25] Kumaravelu G, Alkaisi M M, Bittar A 2002 *29th IEEE Photovoltaic Specialists Conference* New Orleans, LA, USA, May 19–24, 2002 p258

[26] Du L Y 2018 *Ph. D. Dissertation* （Chengdu: University of Electronic Science and Technology of China

[27] Xuan Y Y 2017 *M. S. Thesis* （Chengdu: University of Electronic Science and Technology of China

[28] Khan M, Xu J N, Chen N, Cao W B 2012 *J. Alloys Compd.* **513** 539

[29] Feng J, Xiao B, Chen C J, Zhou C T, Du Y P, Zhou R 2009 *Solid State Commun.* **149** 1569